Nanoscale

PAPER

View Article Online
View Journal | View Issue

Check for updates

Cite this: *Nanoscale*, 2023, **15**, 16687

Biomimetic submicromotor with NIR light triggered motion and cargo release inspired by cuttlefish†

Jiameng Feng,[a] Junjie Zou,*[b] Xiaoyu Li[c] and Xin Du *[a]

Received 30th July 2023,
Accepted 29th September 2023

DOI: 10.1039/d3nr03739h

rsc.li/nanoscale

Biomimetic design is very helpful and significant for the smart construction of micro/nanomotors with artificial intelligence. In this work, inspired by cuttlefish, who can rapidly eject poisonous ink and are also capable of fast movement to escape, we designed and fabricated a biomimetic submicromotor with the ability of simultaneous quick movement and a temperature threshold caused explosive cargo release triggered by near infra-red (NIR) light irradiation, which was approximately equivalent to the action of cuttlefish when encountering a predator. The yolk@shell structured polydopamine@mesoporous silica (PDA@MS_{60}) with immovable and asymmetric yolk distribution was employed as a platform, and this was followed by the simultaneous encapsulation of phase change materials (PCM) and cargo molecules. The NIR light irradiation could not only propel the direct motion of the submicromotor, but also caused the explosive release of the cargo loaded in the submicromotor when the temperature exceeded the melting point of the PCM.

Published on 11 October 2023. Downloaded on 16/10/2025 8:51:46 PM.

1. Introduction

Nature containing a myriad of organisms with evolutionary history is a gigantic laboratory. Organisms in nature that passed the test of natural selection developed their own characteristics and abilities to adapt to the living environment. They often exhibit various interesting survival behaviors according to the changes in environmental factors, such as the group foraging of birds, collective nesting of ants, color changing camouflage of chameleons, ejection of an ink-jet and fast escape of cuttlefish, and so on. Inspired by these creatures, bionic design is used to achieve the optimization of material properties. In the macroscopic world, humans use the shape and movement of animals to create robots with diversity and flexibility, such as the swimming, flying, and crawling inspired by fish, birds, and insects, respectively. In recent years, advanced micro/nanomotors (also called micro/nanorobots) with the capability of movement have aroused significant interest due to their potential abilities for the execution of complex tasks in nanobiomedicine.[1–6] The artificial active systems with biomimetic behaviors are of immense scientific and technological interest for use in artificial intelligence micro/nanomotors. At present, the bionic design has realized the optimization of the motion performance of the micro/nanomotors.[7–12]

Inspired by the swarming behavior of birds, ants, and bacteria in nature, some advanced micro/nanomotors have been designed to realize biomimetic swarming triggered by external stimuli such as magnetism,[13,14] light,[15,16] sound fields,[17] and chemicals.[18,19] For example, peanut-shaped hematite colloidal particles were assembled into ribbons under the action of blue light,[20] and were programmed into liquids, chains, vortex, and ribbon micromotor swarms under an alternating magnetic field, in which the chain-like colloidal particles could pass through a narrow passage.[14] Rod-shaped eutectic gallium–indium alloy liquid metal colloidal motors could self-organize into various strips, circles, and flower-like clusters by modulating the frequency of the applied acoustic field.[17] The titanium oxide (TiO_2) micromotors could achieve clusters and negative phototaxis behavior in aqueous media by electrolyte diffusiophoresis and UV light response, and completed predetermined routes and obstacle avoidance.[21] The combination of two types of micro/nanomotors could lead to the biomimetic predator-prey dynamics. The TiO_2 and zinc oxide (ZnO) particles exhibited an interesting chase-escape motion due to the binary

[a]*Beijing Key Laboratory for Bioengineering and Sensing Technology, Department of Chemistry & Biological Engineering, University of Science & Technology Beijing, Beijing 100083, China. E-mail: duxin@ustb.edu.cn*
[b]*Department of Vascular Surgery, The First Affiliated Hospital of Nanjing Medical University, Nanjing 210029, China. E-mail: zoujunjie@njmu.edu.cn*
[c]*National Engineering Research Center of Green Recycling for Strategic Metal Resources, Key Laboratory of Green Process and Engineering, Institute of Process Engineering, Chinese Academic of Sciences, University of Chinese Academic of Sciences, Beijing 100190, China*

†Electronic supplementary information (ESI) available: Figs. S1–S4, Videos S1 and S2. See DOI: https://doi.org/10.1039/d3nr03739h

Published on 11 October 2023. Downloaded on 16/10/2025 8:51:46 PM.

repulsion-attraction diffusiophoretic interactions.[22] Electro-osmotic flow induced by an ion exchange reaction between ZnO nanorods and sulfonated polybenzenesulfonic acid microbeads resulted in the aggregation of PS microbeads around the ZnO nanorods.[23] Local electrohydrodynamic effect and the photoresponses of the constituents facilitated the leader-follower movement, and the collective positive/negative phototaxis behavior of micropopulations of TiO_2 and silica (SiO_2).[24] Microsphere clusters of a polyelectrolyte-modified SiO_2 with half shells of Pt promoted the aggregation of small clusters towards large clusters due to diffusiophoretic osmotic pressure induced by the decomposition of hydrogen peroxide.[25] In short, these micro/nanomotors were developed with collective intelligence that provides potential solutions for the large-scale and channel-adaptive delivery of drugs in the field of biomedicine. However, the current exploration of biomimetic micro/nanomotors mainly focuses on swarm behavior with self-organization and cooperation capabilities. Up to now, it remains a challenge to design and fabricate micro/nanomotors with high flexibility in responding to stimuli in unfavorable environments to complete a complex task.

Cuttlefish can sense danger when encountering some large animals and predators. Therefore, they will exhibit defensive behavior, that is, they quickly eject poisonous ink from their ink sac to interfere with the smell and sight of the enemy, and also to cover themselves and take the opportunity to move away. Herein, we report the design and fabrication of a novel biomimetic submicromotor, inspired by cuttlefish, with the ability of simultaneous movement and a temperature threshold caused explosive cargo release triggered by NIR light irradiation. It successfully mimics the defensive behavior of natural cuttlefish, which release ink to paralyze enemies and enable them to quickly flee when they confront a high degree of danger. The yolk@shell structured PDA@MS_{60} and NIR light are the equivalent of the cuttlefish and the risk factors (such as predators), and the PCM and doxorubicin (DOX) are equivalent to the ink. When the temperature induced by the NIR light exceeds the melting point of the PCM, this is analogous to a cuttlefish being exposed to danger that exceeds the danger threshold, and the melted PCM with the loaded drugs flows out as quickly as the ink of cuttlefish. The PDA@MS_{60} performs self-propulsion based on self-thermophoresis during the drug release process.

2. Experimental section (materials and methods)

2.1 Reagents

Hexadecyltrimethylammonium chloride (CTAC), chlorobenzene (≥99%), dopamine hydrochloride (≥99%), and doxorubicin (DOX) were purchased from Adama. Triethanolamine (TEA, ≥99%) and tetraethyl orthosilicate (TEOS, ≥99%) were purchased from Sigma-Aldrich. Absolute ethanol (99.5%), aqueous ammonia ($NH_3{\cdot}H_2O$, 28%–30%), and concentrated hydrochloric acid (HCl, 37%) were purchased from Beihua Fine Chemicals. Lauric acid and stearic acid were purchased from Aladdin. The dimethyl sulfoxide (DMSO) was provided by Macklin. The PBS buffer was obtained from Solarbio Science and Technology. All the chemicals were used as received without any further purification. Ultrapure water with a resistivity higher than 18.2 MΩ cm^{-1} was used in all the experiments and was obtained using a three-stage Millipore Milli-Q Plus 185 purification system (academic system).

2.2 Synthesis of core@shell structured PDA@MS_{40} and yolk@shell structured PDA@MS_{60}

The core@shell structured PDA@MS_{40} and yolk@shell structured PDA@MS_{60} were fabricated according to our previously reported work.[26] The mixture of 20 mg of PDA nanospheres (diameter: *ca.* 440 nm), 5 mL of water, and 35 mg of TEA was sonicated for 15 min. Then, the mixture was stirred at a speed of 400 rpm (60 °C), followed by the slow addition of 4 mL of CTAC. After stirring for 1 h, 4.375 mL of chlorobenzene and 0.41 mL of TEOS were added sequentially to the aqueous suspension and kept at 60 °C for 12 h. The yolk@shell PDA@MS_{60} formed was obtained after centrifugation for 3 times at 10 000 rpm, and then twice at 3000 rpm, and washing with water and ethanol (volume ratio of water : ethanol = 1 : 2). The preparation process of the core@shell structured PDA@MS_{40} used the same fabrication procedure as that for the yolk@shell PDA@MS_{60}, except the reaction temperature was 40 °C rather than 60 °C.

The surfactant templates were removed by extraction. The product (100 mg) was dispersed in 15 mL of absolute ethanol (99.5%) and 1 ml of HCl (37%), and then stirred at room temperature for 4 h. The extraction process was repeated twice so that the surfactant was completely removed. After drying at room temperature, the final products were obtained.

2.3 Synthesis of DOX-PDA@MS_{60}

The PDA@MS_{60} (1 mg) was dispersed in a 1 mg mL^{-1} DOX solution (in PBS, pH = 7.4, 10×10^{-3} M) and stirred for 24 h in a dark environment. The DOX-PDA@MS_{60} was collected by centrifugation (10 000 rpm, 10 min) and washed three times with PBS. The obtained DOX-PDA@MS_{60} was dried at 60 °C.

For the loading capacity (LC) of DOX, all the supernatant was collected during the centrifugation and washing, and the residual DOX was determined by using a standard UV-vis adsorption curve measured at 480 nm. The LC of DOX in PDA@MS_{60} was calculated using the following equation:

$$\mathrm{LC} = (M_{\mathrm{ini}} - M_{\mathrm{res}})/M_{\mathrm{pm}} \times 100\%$$

where M_{ini} is the initial amount of DOX, M_{res} is the residual amount of DOX, and M_{pm} is the mass of PDA@MS_{60}.

2.4 Synthesis of PCM-DOX-PDA@MS_{60}

The co-loading of PCM and DOX in PDA@MS_{60} was performed according to a method in the literature.[27] Typically, 5 mg of stearic acid, 20 mg of lauric acid, and 10 mg of DOX were dissolved in 100 μL of DMSO and stirred for 30 min. Then, 4 mg

 This journal is © The Royal Society of Chemistry 2023

Published on 11 October 2023. Downloaded on 16/10/2025 8:51:46 PM.

of PDA@MS_{60} was added to solution and stirred for a further 30 min, and the solution was subsequently stored in a vacuum oven for 12 h to remove the air trapped in the PDA@MS_{60} nanoparticles. Excess fatty acids and DOX were removed by centrifugation (10 000 rpm, 5 min) and two rounds of washing with DMSO. Finally, water was introduced into the precipitate to solidify the fatty acids. The PDA@MS_{60} loaded with a mixture of PCM and DOX was denoted as PCM-DOX-PDA@MS_{60}.

2.5 Release profiles of DOX from DOX-PDA@MS_{60} and PCM-DOX-PDA@MS_{60}

The release profiles of DOX from DOX-PDA@MS_{60} and PCM-DOX-PDA@MS_{60} were investigated under different conditions: (a) the release profile of DOX from PCM-DOX-PDA@MS_{60} at room temperature for 2 h and under NIR light irradiation for 2 h, (b) the release profile of DOX from DOX-PDA@MS_{60} at room temperature for 2 h, (c) the release profile of DOX from DOX-PDA@MS_{60} under NIR light irradiation for 2 h. 1 mL of DOX-PDA@MS_{60} or PCM-DOX-PDA@MS_{60} aqueous suspension (100 μg mL^{-1}) was added into the 2 mL of centrifuge tube, and the contents of the centrifuge tube were stirred at 200 rpm under different NIR light treatment conditions. At different time intervals, 0.5 mL of the suspension was taken out with a syringe filter, and the released DOX was measured using a UV-vis absorption spectrometer. It is worth noting that in order to determine the cumulative amount of DOX released at different time intervals, the suspension after each UV-vis absorption assay was put back into the original centrifuge tube.

2.6 Photothermal conversion measurement

Four different particle concentrations (0, 25, 50, 100 μg mL^{-1}) of the PDA@MS_{60} aqueous suspensions were prepared, and 1 mL of PDA@MS_{60} suspensions were added to the 2.5 mL centrifuge tubes. The heating curves of different concentrations of PDA@MS_{60} suspensions irradiated with 1.5 W cm^{-2} NIR light (808 nm) for 10 min were recorded. It should be noted that there was a distance of *ca.* 4 cm between the NIR light window and the centrifuge tube. A digital thermometer with a 4-channel thermocouple data logger (RDXL4SD, Omega Engineering) was used to monitor the temperature change. The head of the thermometer was completely immersed in the solution, and the temperature change was recorded at 2 s intervals.

In order to achieve the expected drug release effect of PCM-DOX-PDA@MS_{60}, we systematically considered the results of the heating curves of the previous four particle concentrations of PDA@MS_{60}, and 100 μg mL^{-1} was selected as the particle concentration. The heating curves of 1 mL of DOX-PDA@MS_{60} and 1 mL of PCM-DOX-PDA@MS_{60} under 1.5 W cm^{-2} NIR light irradiation for 2 h were obtained. In order to monitor the cumulative release of DOX from DOX-PDA@MS_{60} and PCM-DOX-PDA@MS_{60} over 2 h with the change of temperature rise in real time, we quickly removed 0.5 mL of particle suspension at different time intervals during the UV-vis absorption analysis, and the tested particle suspension was added back into the temperature-monitored centrifuge tube. The previously mentioned operation process inevitably caused the phenomenon where the temperature at different time intervals dropped by different amounts.

2.7 Characterization of the NIR light propulsion

The PDA@MS_{60}, DOX-PDA@MS_{60}, and PCM-DOX-PDA@MS_{60} in 10 μL of water were added to a groove (5 mm diameter, 0.5 mm thickness) on the quartz glass slide (2 mm thickness) and sealed with a highly cleaned cover glass (8 mm diameter) to avoid environmental disturbances. In addition, the edge of the cover glass that was in contact with the slide was painted with nail Polish to avoid the influence of liquid evaporation caused by the photothermal effect on the movement. An 808 nm fiber-coupled diode laser system was used to provide a gradient of the NIR light irradiation to trigger the submicromotors. All the imaging experiments were recorded at a rate of 10 frames per second using a Nikon 80i upright microscope, which was equipped with a 100 W halogen tungsten lamp, a 20× Plan Fluor objective, and a CCD camera. We used ImageJ and its plug-in (TrackMate) to analyze the motion of the submicromotors.

2.8 Characterization

Scanning electron microscopy (SEM) was performed on a Hitachi SU8010 SEM at 10 kV and 10 μA. Before the SEM measurements, the sample surface was coated by ion sputtering with a layer of gold with a size of 5 nm. Field-emission scanning electron microscopy (FE-SEM) observations were performed on a Hitachi SU8010 FE-SEM. For dual beam (electron beam and focused ion beam (FIB)) scanning electron microscopy (FIB-SEM) imaging, the particles were drop-coated on a silica wafer, and platinum was coated on the surface of the particles. A Ga ion beam was used to cut the coated particles, which were observed using a ThermoScientific Helios G5 CX FIB-SEM. Before the observations, gold was sputtered on the sample to improve the sample conductivity. The samples dispersed in ethanol were dripped onto a carbon-coated copper grid, and observed under a Hitachi HT7700 transmission electron microscope (TEM) at an accelerating voltage of 100 kV. The UV-visible absorption spectra in the wavelength range of 200–600 nm were measured with a Shimadzu UV-1800 spectrophotometer, and the UV-visible absorbance at a characteristic absorption peak of DOX (480 nm) was recorded by wave point measurement during the DOX release process.

3. Results and discussion

Based on our previously developed strategy of temperature regulated swelling and restricted asymmetric shrinkage of PDA nanospheres,[26] combined with heterogeneous interface self-assembly growth, yolk@shell structured PDA@MS_{60} with immovable and asymmetric yolk distribution was fabricated and employed as a carrier platform (Fig. 1a). The eutectic mixture of lauric acid and stearic acid as the PCM, and DOX as

Published on 11 October 2023. Downloaded on 16/10/2025 8:51:46 PM.

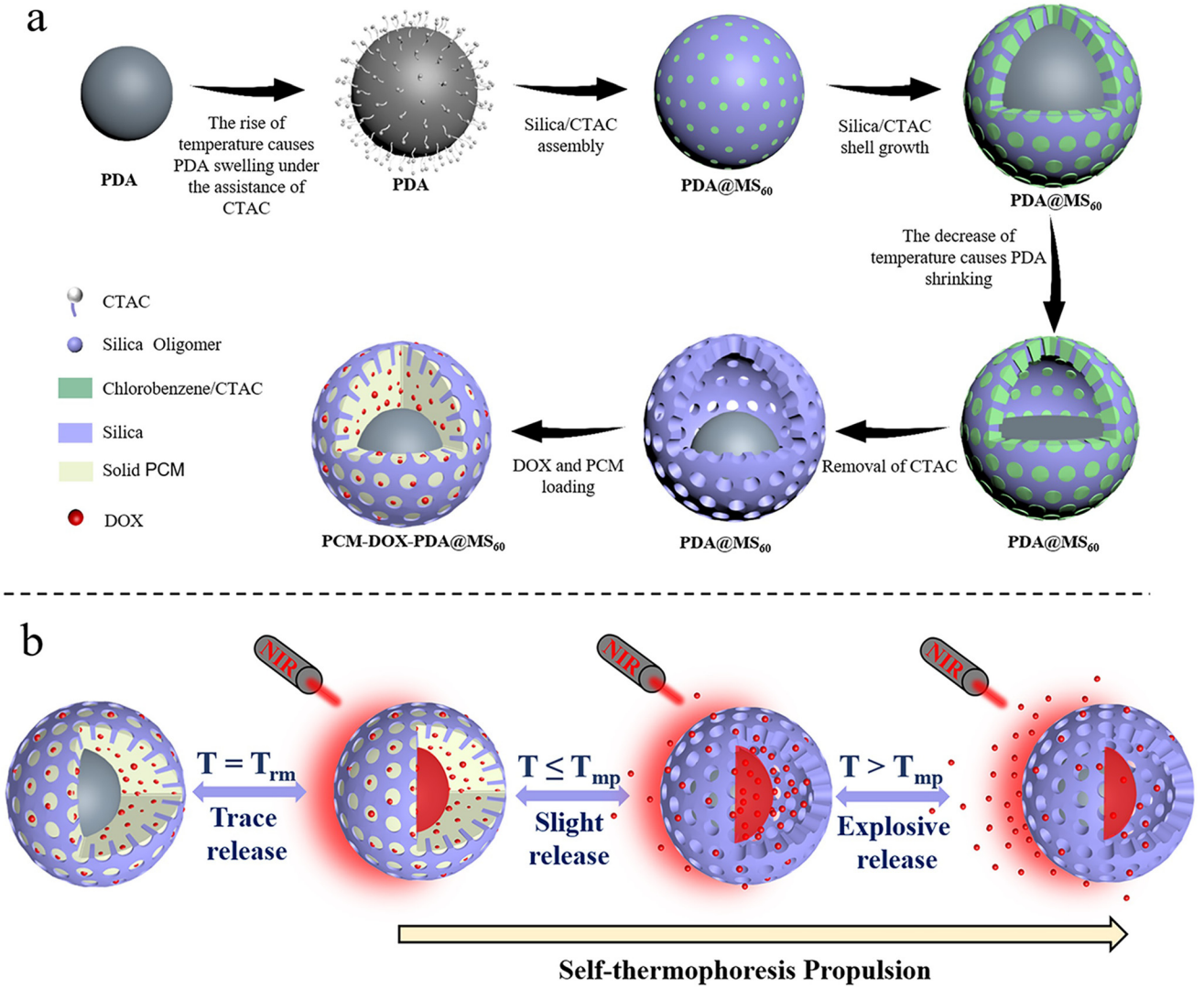

Fig. 1 Schematic illustrations of (a) the fabrication of the yolk@shell structured PCM-DOX-PDA@MS_{60} with immovable and asymmetric yolk distribution, and (b) the NIR light-triggered propulsion of PCM-DOX-PDA@MS_{60} *via* a self-thermophoresis mechanism, combined with temperature threshold responsive DOX release.

cargo molecules were simultaneously loaded in the pores and hollow cavity of PDA@MS_{60} (Fig. 1a). The encapsulation of DOX in PDA@MS_{60} was realized by utilizing the characteristics of PCM to solidify when exposed to water. The constructed PCM-DOX-PDA@MS_{60} nanocomposite became a biomimetic cuttlefish-like fuel-free colloidal submicromotor, which had the capacity for NIR light-triggered two directional particle motion and temperature threshold responsive cargo release (Fig. 1b). Under the NIR light irradiation with a fixed direction, the asymmetrical distribution of the PDA yolk, with excellent photothermal properties, confined within the mesoporous silica shell formed the local asymmetrical temperature gradient around the nanocomposite to propel the direct motion of the submicromotor by a self-thermophoresis mechanism. Simultaneously, under the NIR light irradiation, the temperature of the PCM-DOX-PDA@MS_{60} aqueous suspension gradually increased with time. Together with the temperature changes from room temperature (T_{rm}) to the melting point (T_{mp}) of PCM, then to the melting point, the DOX release varied from trace to slight, then to explosive (Fig. 1b). The explosive DOX release combined with a quick movement was similar to the rapid ejection of the poisonous ink from the ink sac of cuttlefish together with its escape using fast movements.

3.1 Materials characterization

The PDA@MS nanocomposites with two different structures of core@shell and yolk@shell were fabricated by using PDA nanospheres of *ca.* 440 nm (Fig. S1, ESI†) as a core at different reaction temperatures of 40° and 60 °C. As shown in Fig. 2a and b, the PDA@MS_{40} nanocomposites had a uniform spherical core@mesoporous shell structure with a particle size of *ca.*

 This journal is © The Royal Society of Chemistry 2023

Published on 11 October 2023. Downloaded on 16/10/2025 8:51:46 PM.

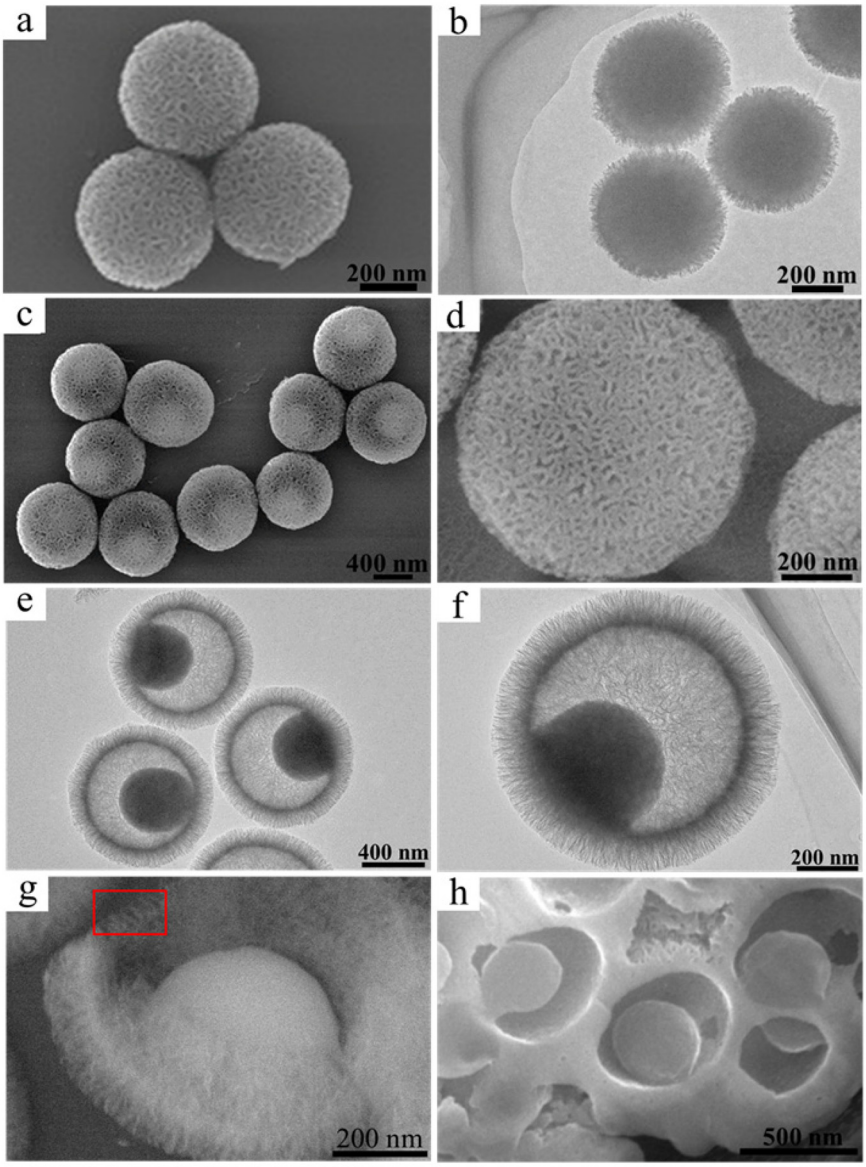

Fig. 2 The SEM (a) and TEM (b) images of core@shell structured PDA@MS_{40}, the SEM (c) and (d) and TEM (e) and (f) images of yolk@shell structured PDA@MS_{60}, the SEM image of a broken yolk@shell structured PDA@MS_{60} (g), and the FIB-SEM image of the yolk@shell structured PDA@MS_{60} (h).

500 ± 25 nm. In comparison, the PDA@MS_{60} nanocomposites formed had a uniform spherical yolk@mesoporous shell structure with a particle size of *ca.* 820 ± 30 nm (Fig. 2c–h, and S2, ESI†). The sizes of the mesopores on the sphere surface were in the range of 3–27 nm (Fig. 2c and d). The arrangement of the mesopores in the shell shows a radial pattern in the center and the thickness of mesoporous shell was *ca.* 120 nm (Fig. 2e and f). As shown by the area in the red rectangular frame of the SEM image (Fig. 2g) of a broken yolk@shell structured PDA@MS_{60}, the straight mesopore channels in the shell penetrated through both the inside and the outside, indicating the permeability of mesoporous shell. In addition, the FIB-SEM image in Fig. 2h shows that the PDA yolk is fixed onto the inner surface of the shell. The energy dispersive X-ray spectroscopy (EDX) elemental mapping images of PDA@MS_{60} shown in Fig. S3 (ESI†) show that the abundance and the distribution areas of the C and N elemental compositions mainly lie in the PDA core.

3.2 Cargo loading capacity and photothermal property

Without the introduction of PCM, the DOX loading capacity, by the UV-vis adsorption method, in the PDA@MS_{60} was *ca.* 59.3 ± 4.0%. It is worth noting that the loading rate can slightly fluctuate because of the inevitable operational error during the experiment (Fig. S4 and Tables S1–S3, ESI†). The high loading capacity can be attributed to the cavity, and the large (3–27 nm) and penetrative pore channel from the cavity to exterior (Fig. 2c, d and g). Compared with the PDA@MS_{60} in the TEM image (Fig. 3a), there exists some faintly visible flocculent substance (Fig. 3b) in the DOX-PDA@MS_{60}, which could

Published on 11 October 2023. Downloaded on 16/10/2025 8:51:46 PM.

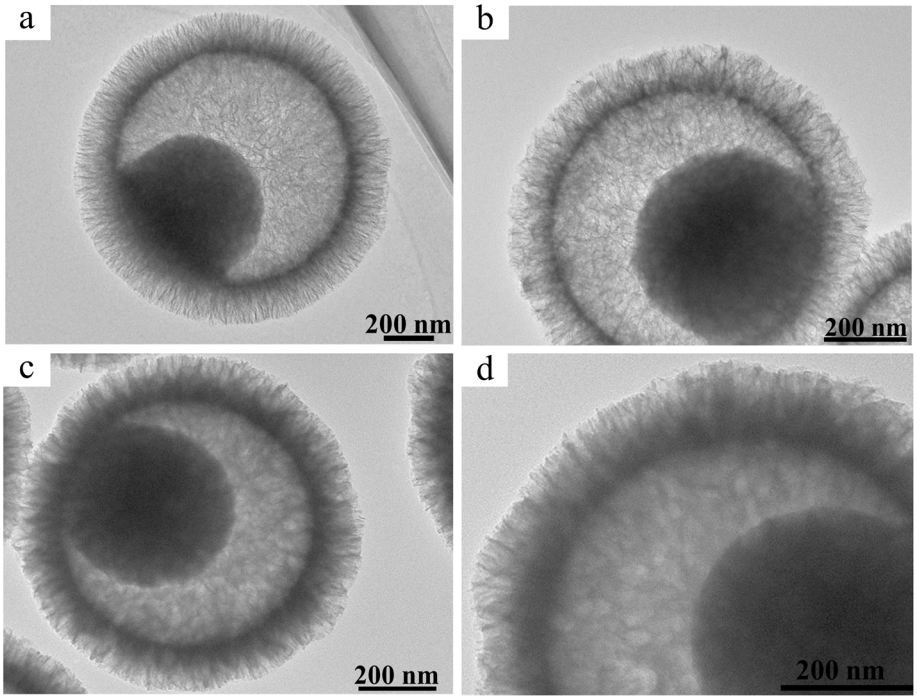

Fig. 3 The TEM images of (a) PDA@MS_{60}, (b) DOX-PDA@MS_{60} with a DOX loading capacity of 65.0%, and (c) and (d) the PCM-DOX-PDA@MS_{60} with a DOX loading capacity of 13.4%.

be attributed to the loading of a large amount of DOX organic molecules. In comparison, when PCM and DOX were simultaneously loaded in the PDA@MS_{60}, the DOX loading capacity decreased from 59.3 ± 4.0% to 13.4 ± 2.1% in the PCM-DOX-PDA@MS_{60} because of the competitive space occupation of PCM in the PDA@MS_{60}. The TEM images in Fig. 3c and d show that the color of the PCM-DOX-PDA@MS_{60} became darker, and the mesopores in the shell became blurrier, which suggested the loading of more organic species in the PDA@MS_{60}.

Next, we investigated the photothermal property of PDA@MS_{60}. As shown in Fig. 4a and b, all the curves exhibited a tendency to have a time-dependent temperature rise with a gradual slowing down of the increasing speed under the NIR light irradiation. Clearly, it was found that a higher power density resulted in a higher temperature increase effect. Under NIR light irradiation (808 nm, 1.5 W cm^{-2}), the pure water only had a low temperature rise of *ca.* 8.4 °C from 26.0 °C to 34.4 °C in 10 min. In contrast, the temperature of the PDA@MS_{60} aqueous suspensions rapidly increased from 26 °C to 39.3, 43.5, and 47.7 °C for the increased particle concentrations of 25, 50, and 100 μg mL^{-1}, respectively (Fig. 4a), which was in agreement with a particle concentration-dependent temperature increase. Considering that melting is an endothermic process, the temperature of the PCM-loaded PDA@MS_{60} reached will be lower at the same particle concentration and laser power than that of the PDA@MS_{60}. Therefore, a relatively high power density and high particle concentration

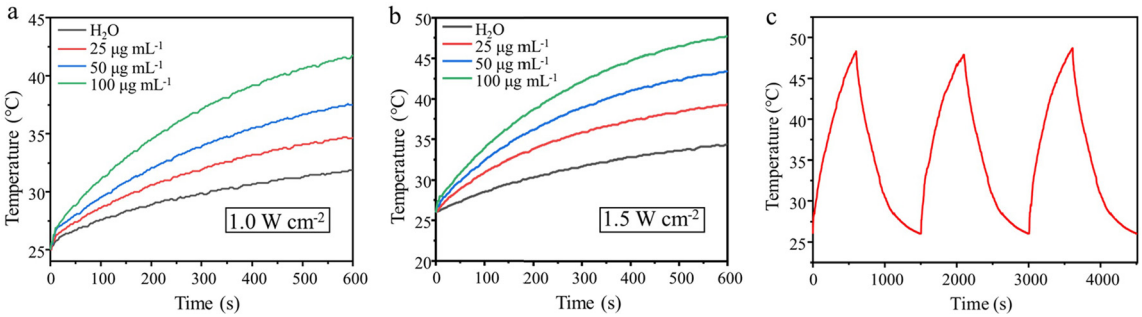

Fig. 4 The temperature change profiles of water and PDA@MS_{60} aqueous suspensions with different particle concentrations (25, 50, and 100 μg mL^{-1}) under 808 nm NIR laser irradiation with different power densities of (a) 1.0 and (b) 1.5 W cm^{-2}. (c) The temperature change profile of the PDA@MS_{60} aqueous suspension (100 μg mL^{-1}) under 808 nm NIR laser irradiation (1.5 W cm^{-2}, 10 min) with the light turned on/off for three cycles.

This journal is © The Royal Society of Chemistry 2023

Published on 11 October 2023. Downloaded on 16/10/2025 8:51:46 PM.

(1.5 W cm^{-2}, 100 μg mL^{-1}) should be chosen to elevate the temperature of the aqueous particle suspensions to exceed the melting point (42.0–43.1 °C) of PCM (Fig. S5e and S5e', ESI†). In addition, with three cycles of turning NIR laser on/off, the PDA@MS_{60} aqueous suspension shows three almost identical heating and cooling profiles (Fig. 4c), demonstrating its high photothermal conversion stability. In addition, the morphology and structure of the PDA@MS_{60} were well preserved after three cycles of NIR laser-induced temperature change, showing the good thermal stability of the structure (Fig. S6, ESI†).

3.3 The NIR light propelled motion behavior

Under the NIR light irradiation, the asymmetrically distributed PDA yolk, with an excellent photothermal conversion property, confined within the mesoporous silica shell should generate a local thermal gradient field around the PDA@MS, thus triggering the particle motion by a self-thermophoretic mechanism.[28–32] Two types of PDA@MSs with core@shell and yolk@shell structures were chosen to investigate the effect of different nanostructures on the thermophoretic propulsion. Compared with irregular Brownian movement in the absence of NIR light, all of their movement trajectories were obviously prolonged under NIR light irradiation (Fig. 5a and Video S1, ESI†). The calculated mean square displacement (MSD) of particle Brownian motion increases linearly with the time interval (Δt) (Fig. 5b and c), which indicated a random diffusion motion form. The increased slopes of the MSD curves (Fig. 5b and c) indicated the enhanced diffusion of the PDA@MSs irradiated by NIR light. It is worth noting that the PDA@MS_{60} had a higher MSD than PDA@MS_{40} under identical conditions (Fig. 5b and c). Furthermore, it was found that the MSD curves of the PDA@MS_{60} exhibited a tendency of a slight parabolic increase under the irradiation of NIR light with high power densities of 1.5 and 2.0 W cm^{-2} (Fig. 5c), indicating that the NIR light irradiation can slightly improve the directionality of the PDA@MS_{60} motion. The effective diffusion coefficient (D_e) was calculated using the equation: D_e = MSD/4Δt to compare the movement of the PDA@MS_{40} and PDA@MS_{60}. As shown in Fig. 5d, PDA@MS_{60} has a higher D_e than PDA@MS_{40} under identical conditions. Under the irradiation of NIR light with high power densities of 1.5 and 2.0 W cm^{-2}, the D_e values of PDA@MS_{60} were almost twice (2.45 *vs.* 1.23, 3.02 *vs.* 1.53) those of PDA@MS_{40} (Fig. 5d). The results of MSD and D_e indicate that the yolk@shell structure is more favorable for generating the asymmetric local thermal gradient field for the NIR light-propelled particle motion than core@shell structure,[28–32] although the yolk@shell structured PDA@MS_{60} has a larger particle size (820 ± 30 nm *vs.* 500 ± 25 nm) and lower PDA content (*i.e.*, a lower photothermal conversion property), which was detrimental to the rapid motion of the particles. After DOX and PCM were loaded into the PDA@MS_{60}, the PCM-DOX-PDA@MS_{60} also exhibited a power density-dependent increase of MSD (Fig. 5e and Video S2, ESI†), but it had a slightly lower MSD (Fig. 5c and e) and D_e (Fig. 5d) than PDA@MS_{60}. This should be mainly attributed to the increase

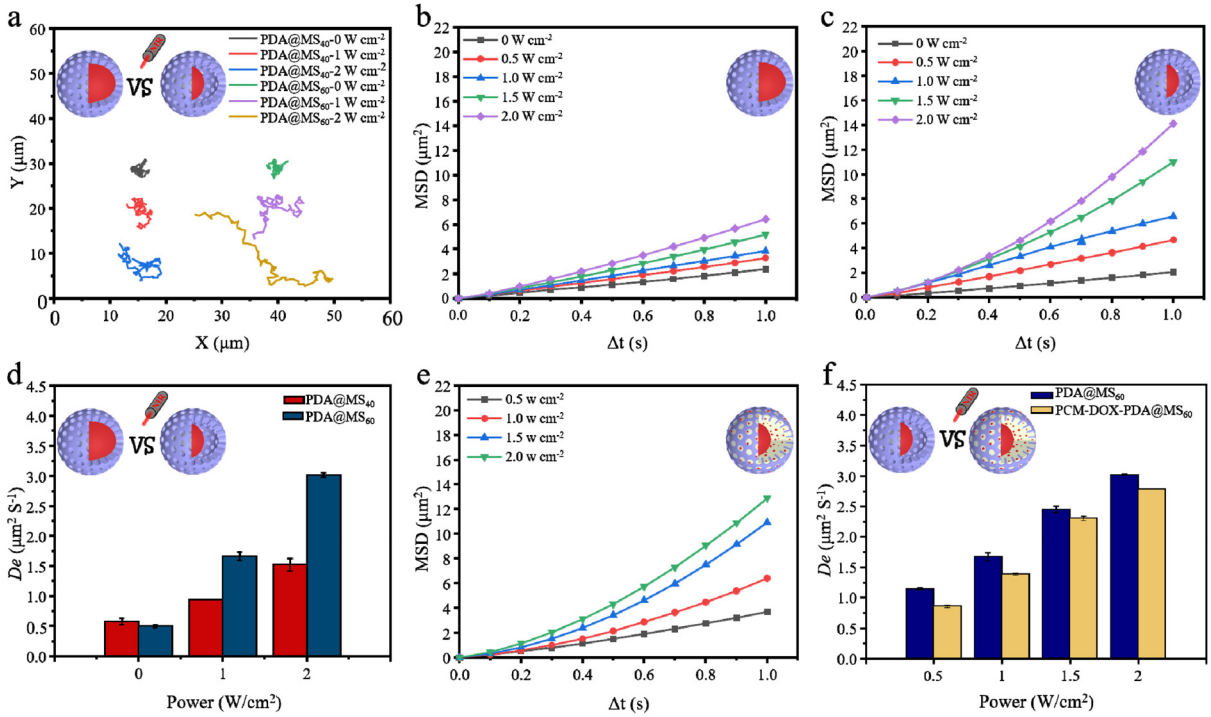

Fig. 5 (a) The trajectories of PDA@MS_{40} and PDA@MS_{60} with or without the irradiation of NIR light with different power densities in 10 to 20 s. The MSD of (b) PDA@MS_{40} and (c) PDA@MS_{60}. (d) The D_e of PDA@MS_{40} and PDA@MS_{60}. (e) The MSD of PCM-DOX-PDA@MS_{60}. (f) The D_e of PDA@MS_{60} and PCM-DOX-PDA@MS_{60}.

Published on 11 October 2023. Downloaded on 16/10/2025 8:51:46 PM.

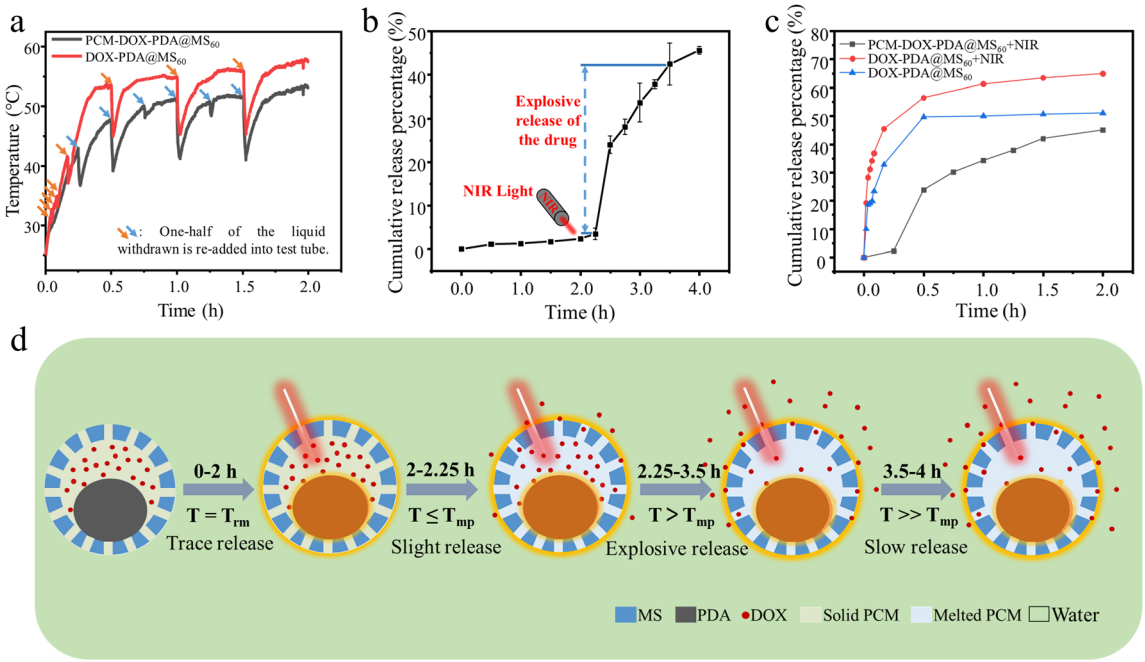

Fig. 6 (a) The temperature change profiles of PCM-DOX-PDA@MS_{60} and DOX-PDA@MS_{60} aqueous suspensions (100 μg mL^{-1}) under 808 nm NIR laser irradiation (1.5 W cm^{-2}) for 2 h. (b) The cumulative DOX release profile from PCM-DOX-PDA@MS_{60} in water under room temperature for 2 h and NIR light irradiation (808 nm, 1.5 W cm^{-2}) for 2 h. The data error bars indicate mean ± SD (n = 3). (c) Cumulative DOX release profiles from DOX-PDA@MS_{60} in water with or without NIR laser irradiation (880 nm, 1.5 W cm^{-2}, 2 h), and PCM-DOX-PDA@MS_{60} in water with NIR laser irradiation (880 nm, 1.5 W cm^{-2}, 2 h). (d) The schematic illustration of the possible DOX release from PCM-DOX-PDA@MS_{60} in water at different temperatures.

of the PCM-DOX-PDA@MS_{60} weight, the decrease of PDA content in PCM-DOX-PDA@MS_{60}, and the loss of heat transfer from PDA to PCM.

3.4 Cuttlefish-like submicromotor with NIR light triggered motion and cargo release

After 808 nm NIR laser irradiation (1.5 W cm^{-2}) for 2 h, the temperature of the DOX-PDA@MS_{60} and PCM-DOX-PDA@MS_{60} aqueous suspensions (100 μg mL^{-1}) increased from 25 °C to 57.7 °C and 53.3 °C, respectively (Fig. 6a). The sudden decrease in the temperature change profiles was ascribed to the re-addition of one-half of the liquid withdrawn for UV-vis adsorption measurement. Together with the temperature change shown in Fig. 6a, the cumulative DOX release profile from PCM-DOX-PDA@MS_{60} in Fig. 6b shows a phenomenon where there was a slow DOX release of *ca.* 2.38% during the initial 0–2 h without NIR light irradiation (at room temperature), and then a relatively quick DOX release of *ca.* 1.09% during the next 2–2.25 h with NIR light irradiation (from 25.0 to 43.0 °C), next a quick DOX release of *ca.* 38.96% during 2.25–3.5 h (from 43.0 to 51.5 °C), and finally a slowed DOX release of *ca.* 2.60% during 3.5–4 h (from 51.5 to 53.3 °C). It should be noted that the explosive release of DOX begins at 43.0 °C, which corresponds to the completely melted temperature of the PCM with the melting point of PCM being 42.0–43.1 °C (Fig. S5, ESI†). The digital images in Fig. S4 (ESI†) show the corresponding color change of the PCM-DOX-PDA@MS_{60} aqueous suspension from colorless to light red, then to a relatively deepened red, finally to an almost unchanged red at different times during the DOX release process under NIR light irradiation, which was largely consistent with the DOX release situation. In contrast, without the introduction of PCM, as shown in Fig. 6c, the DOX release from the PDA@MS_{60} exhibits an explosive form of *ca.* 49.72% during the initial 0–0.5 h without NIR light irradiation, followed by a slow release of *ca.* 1.39% during the next 0.5–2 h. Under the NIR light irradiation, more DOX molecules can be released from PDA@MS_{60} with a cumulative release percentage of *ca.* 64.97% at 2 h (Fig. 6c), which was mainly due to the thermal effect. Based on these phenomena, shown in Fig. 6a–c, the schematic illustration in Fig. 6d shows the possible DOX release situation from PCM-DOX-PDA@MS_{60} in water at different temperatures: from trace to slight, then to explosive, finally to slow release. The explosive cargo release could be attributed to the fact that when the temperature of the PCM-DOX-PDA@MS_{60} aqueous suspension induced by the NIR light irradiation exceeds the melting point of PCM, the melted PCM begins to flow out through the permeable mesopores of the silica shell, resulting in the explosive DOX release. The explosive cargo release is similar to the rapid ejection of the poisonous ink from the ink sac of cuttlefish. Therefore, the constructed PCM-DOX-PDA@MS_{60} nanocomposite becomes a biomimetic cuttlefish-like fuel-free colloidal submicromotor, which has the capacity of both quick directional particle

 This journal is © The Royal Society of Chemistry 2023

Published on 11 October 2023. Downloaded on 16/10/2025 8:51:46 PM.

motion and temperature threshold-responsive cargo release triggered by NIR light irradiation of a fixed direction.

4. Conclusions

In this work, we fabricated a biomimetic cuttlefish-like fuel-free colloidal submicromotor by loading PCM and DOX in the yolk@shell structured PDA@MS_{60}. The NIR light irradiation propelled the direct motion of the submicromotor by a self-thermophoresis mechanism, and simultaneously caused the explosive release of the cargo loaded in the submicromotor when the temperature exceeded the melting point of PCM. When the NIR light irradiation was approximately equivalent to the predator of cuttlefish, the behavior of the NIR light triggered simultaneous temperature threshold caused explosive cargo release and a quick movement, which is similar to the rapid ejection of the poisonous ink from cuttlefish, together with its fast movement for escaping. Such a cuttlefish-like submicromotor offers an interesting biomimetic design strategy. The combination of this biomimetic thermally responsive system with the active propulsion system will provide an ingenious design for controlled drug delivery. However, our exploration is currently limited to proof-of-concept, and the microenvironmental adaptation and drug delivery effect remain unclear *in vivo*. It is expected that this type of submicromotor will act as an intelligent nanorobot for various biomedical applications in the near future.

Conflicts of interest

The authors declare no conflict of interest.

Acknowledgements

This work is supported by the National Natural Science Foundation of China (Grant No. 51971208), the Youth Innovation Promotion Association CAS, the Fundamental Research Funds for the Central Universities (Grant No. FRF-BD-20-14A), and the Beijing Municipal Science and Technology Commission (Grant No. z131102002813058).

References

1 T. Y. Liu, L. Xie, C. A. H. Price, J. Liu, Q. He and B. Kong, *Chem. Soc. Rev.*, 2022, **51**, 10083–10119.
2 A. Aziz, S. Pane, V. Iacovacci, N. Koukourakis, J. Czarske, A. Menciassi, M. Medina-Sanchez and O. G. Schmidt, *ACS Nano*, 2020, **14**, 10865–10893.
3 C. Y. Gao, Y. Wang, Z. H. Ye, Z. H. Lin, X. Ma and Q. He, *Adv. Mater.*, 2021, **33**, 2000512.
4 J. Wang, Y. Dong, P. Ma, Y. Wang, F. Y. Zhang, B. C. Cai, P. Chen and B. F. Liu, *Adv. Mater.*, 2022, **34**, 2201051.
5 W. Liu, Y. Liu, H. Li, H. M. Nie, M. Y. Tian and W. Long, *Adv. Funct. Mater.*, 2023, **33**, 2212452.
6 M. Yan, L. Xie, J. Y. Tang, K. Liang, Y. F. Mei and B. A. Kong, *Chem. Mater.*, 2021, **33**, 3022–3046.
7 I. Buttinoni, J. Bialke, F. Kummel, H. Lowen, C. Bechinger and T. Speck, *Phys. Rev. Lett.*, 2013, **110**, 238301.
8 S. Hernandez-Navarro, P. Tierno, J. A. Farrera, J. Ignes-Mullol and F. Sagues, *Angew. Chem., Int. Ed.*, 2014, **53**, 10696–10700.
9 M. Driscoll, B. Delmotte, M. Youssef, S. Sacanna, A. Donev and P. Chaikin, *Nat. Phys.*, 2017, **13**, 375–379.
10 H. Massana-Cid, F. Martinez-Pedrero, E. Navarro-Argemi, I. Pagonabarraga and P. Tierno, *New J. Phys.*, 2017, **19**, 103031.
11 G. Kokot and A. Snezhko, *Nat. Commun.*, 2018, **9**, 2344.
12 H. J. Zhou, C. C. Mayorga-Martinez, S. Pane, L. Zhang and M. Pumera, *Chem. Rev.*, 2021, **121**, 4999–5041.
13 J. Yan, K. Chaudhary, S. C. Bae, J. A. Lewis and S. Granick, *Nat. Commun.*, 2013, **4**, 1516.
14 H. Xie, M. M. Sun, X. J. Fan, Z. H. Lin, W. N. Chen, L. Wang, L. X. Dong and Q. He, *Sci. Robot.*, 2019, **4**, eaav8006.
15 Y. Y. Hong, M. Diaz, U. M. Cordova-Figueroa and A. Sen, *Adv. Funct. Mater.*, 2010, **20**, 1568–1576.
16 S. M. Fu, D. M. Fu, D. Z. Xie, L. Liu, B. Chen, Y. C. Ye, D. A. Wilson and F. Peng, *Appl. Mater. Today*, 2022, **26**, 101348.
17 Z. S. Li, H. Y. Zhang, D. L. Wang, C. Y. Gao, M. M. Sun, Z. G. Wu and Q. He, *Angew. Chem., Int. Ed.*, 2020, **59**, 19884–19888.
18 D. Kagan, S. Balasubramanian and J. Wang, *Angew. Chem., Int. Ed.*, 2011, **50**, 503–506.
19 A. Altemose, M. A. Sanchez-Farran, W. T. Duan, S. Schulz, A. Borhan, V. H. Crespi and A. Sen, *Angew. Chem., Int. Ed.*, 2017, **56**, 7817–7821.
20 Z. H. Lin, T. Y. Si, Z. G. Wu, C. Y. Gao, X. K. Lin and Q. He, *Angew. Chem., Int. Ed.*, 2017, **56**, 13517–13520.
21 F. Z. Mou, J. H. Zhang, Z. Wu, S. N. Du, Z. X. Zhang, L. L. Xu and J. G. Guan, *iScience*, 2019, **19**, 415–424.
22 F. Z. Mou, X. F. Li, Q. Xie, J. H. Zhang, K. Xiong, L. L. Xu and J. G. Guan, *ACS Nano*, 2020, **14**, 406–414.
23 C. J. Wu, J. Dai, X. F. Li, L. Gao, J. Z. Wang, J. Liu, J. Zheng, X. J. Zhan, J. W. Chen, X. Cheng, M. C. Yang and J. Y. Tang, *Nat. Nanotechnol.*, 2021, **16**, 288–295.
24 X. Liang, F. Z. Mou, Z. Huang, J. H. Zhang, M. You, L. L. Xu, M. Luo and J. G. Guan, *Adv. Funct. Mater.*, 2020, **30**, 1908602.
25 T. Y. Si, Z. W. Wu, W. P. He and Q. He, *iScience*, 2023, **26**, 106112.
26 M. H. Qiao, Y. Xing, L. Xie, B. Kong, F. Kleitz, X. Y. Li and X. Du, *Small*, 2022, **18**, 2205576.
27 N. Wang, H. Y. Chen, L. Lin, Y. Zhao, X. Y. Cao, Y. L. Song and L. Jiang, *Macromol. Rapid Commun.*, 2010, **31**, 1622–1627.
28 Y. J. Wu, T. Y. Si, J. X. Shao, Z. G. Wu and Q. He, *Nano Res.*, 2016, **9**, 3747–3756.

29 J. Y. Lv, Y. Xing, T. L. Xu, X. J. Zhang and X. Du, *Appl. Mater. Today*, 2021, **23**, 101034.
30 Y. Xing, S. S. Tang, X. Du, T. L. Xu and X. J. Zhang, *Nano Res.*, 2021, **14**, 654–659.
31 L. Xie, T. Y. Liu, Y. J. He, J. Zeng, W. Zhang, Q. R. Liang, Z. L. Huang, J. Y. Tang, K. Liang, L. Jiang, O. Terasaki, D. Y. Zhao and B. Kong, *Angew. Chem., Int. Ed.*, 2022, **61**, e202200240.
32 L. Xie, M. Yan, T. Y. Liu, K. Gong, X. Luo, B. L. Qiu, J. Zeng, Q. R. Liang, S. Zhou, Y. J. He, W. Zhang, Y. L. Jiang, Y. Yu, J. Y. Tang, K. Liang, D. Y. Zhao and B. A. Kong, *J. Am. Chem. Soc.*, 2022, **144**, 1634–1646.

Published on 11 October 2023. Downloaded on 16/10/2025 8:51:46 PM.

This journal is © The Royal Society of Chemistry 2023